

Research Article

Deformation Reconstruction and High-Precision Attitude Control of a Launch Vehicle Based on Strain Measurements

Liang Zhuang ¹ and Zhang Yulin ^{1,2}

¹*School of Aerospace Science and Technology, National University of Defense Technology, Changsha, China 410073*

²*School of Control Science and Engineering, Zhejiang University, Hangzhou, China 310027*

Correspondence should be addressed to Liang Zhuang; liangzhuang15@nudt.edu.cn

Received 5 November 2020; Revised 16 December 2020; Accepted 15 January 2021; Published 8 February 2021

Academic Editor: Paolo Gasbarri

Copyright © 2021 Liang Zhuang and Zhang Yulin. This is an open access article distributed under the Creative Commons Attribution License, which permits unrestricted use, distribution, and reproduction in any medium, provided the original work is properly cited.

The development of launch vehicles has led to higher slenderness ratios and higher structural efficiencies, and the traditional control methods have difficulty in meeting high-quality control requirements. In this paper, an incremental dynamic inversion control method based on deformation reconstruction is proposed to achieve high-precision attitude control of slender launch vehicles. First, the deformation parameters of a flexible rocket are obtained via fiber Bragg grating (FBG) sensors. The deformation and attitude information is introduced into the incremental dynamic inverse control loop, and an attitude control framework that can alleviate bending vibration and deformation is established. The simulation results showed that the proposed method could accurately reconstruct the shapes of flexible launch vehicles with severe vibration and deformation, which could improve the accuracy and stability of attitude control.

1. Introduction

To improve launch capacity, the development trend of launch vehicles is to increase the slenderness ratio and reduce the structural mass; thus, the structural vibrations and flexible characteristics of rockets are becoming increasingly significant. During a flight process, a large vibration amplitude will not only damage the structure of the rocket but also lead to inaccurate information measured by the attitude sensors. In addition, the low-order vibration modes of the rocket are easily excited by external interference, which has a negative impact on the stability of the rocket [1].

To prevent structural vibration signals from feeding back to the trajectory control system, some effective strategies have been adopted including notch filters [2–5] and observers [6, 7]. Choi and Bang [2, 3] designed an adaptive notch filter that first estimated the elastic mode frequency and then adjusted the notch filter parameters based on the identification results to improve the control performance. Oh et al. [4] proposed an attitude control method with real-time control adaptive notch filter technology and developed a demonstration sys-

tem to verify the stability of the method. Wei et al. [5] introduced an adaptive filtering attitude control algorithm and a norm robust gain scheduling control algorithm to design the controller and verified the effectiveness and robustness of the two control methods. Shtessel and Baev [6] realized the separation and reconstruction of the first two modes of the rocket body using a sliding mode observer and introduced the modal information into the control loop. Zhou et al. [7] applied a robust state observer to the attitude stability control of a launch vehicle and realized antijamming attitude controller design through the observation and compensation of the compound interference.

The research of the above scholars mainly focused on two strategies to deal with the attitude control problem caused by the vibration of the projectile: the first is to use the robustness of the controller to suppress flexible interference without using any structural filters and the second is to design a notch filter to suppress the vibration modes. Although robust control can achieve stable flight, the design parameters are generally conservative, and the control accuracy is low. The use of a notch filter will reduce the phase margin, and it is

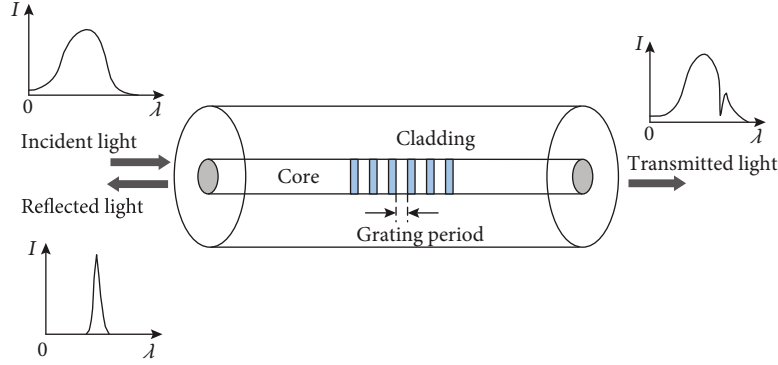


FIGURE 1: FBG measurement principle diagram.

difficult to ensure that the rigid and elastic rocket bodies have a sufficient stability margin at the same time [6]. It is difficult to meet the requirements of launch vehicle development using only attitude information. Therefore, it is necessary to measure the strain and deformation of the rocket body and introduce the deformation information into the control system to achieve high-precision attitude control and stable flight of the rocket.

The fiber Bragg grating (FBG) has various advantages, including a small size, low weight, antielectromagnetic interference, and multiplexing capabilities [8]. In recent years, optical fiber sensor systems have been used for structural monitoring and diagnosis [9–11], and they have been applied in the development of aircraft and launch vehicles at NASA's Armstrong Flight Research Center and Kennedy Space Center [12]. By installing a fiber Bragg grating sensor array on the rocket body to measure the rocket strain, the stress and deformation state of the rocket structure, decoupling attitude, and elastic deformation information can be obtained in real time to obtain accurate rocket attitude information. Combined with an advanced control algorithm, the accuracy and stability of rocket attitude control can be effectively improved. At present, there are some research results in the field of rocket deformation reconstruction and attitude control using fiber Bragg grating sensors, but they mainly focus on the deformation reconstruction algorithm of the rocket [12–14]. To the authors' knowledge, at present, comprehensive research of the combination of rocket deformation and attitude control has not been carried out.

To solve the problem of high-precision attitude control of a flexible rocket, a high-precision attitude control method is proposed in this paper, which introduces the deformation and attitude information into the control loop. In the deformation reconstruction of the rocket, the basic theory and method of shape reconstruction using a fiber Bragg grating sensor are studied. The proposed reconstruction method is applied to the bending vibration analysis of a cantilever beam, and the accuracy of the method is verified by comparing with the modal displacement and angular velocity of the cantilever beam obtained by finite element simulations. In the design of a flexible-body rocket attitude controller, the dynamic model of a flexible-body rocket is established. Based on incremental nonlinear dynamic inversion (INDI), the

deformation information is introduced into the design of the attitude controller. An FBG+INDI control strategy is proposed, and the effectiveness and robustness of the proposed control scheme are verified.

2. Deformation Reconstruction Method of a Flexible Launch Vehicle

2.1. Principle of Strain Sensing with FBG. Fiber Bragg grating (FBG) sensing technology is essentially a new type of sensing technology that uses the Bragg grating effect to sense physical quantities such as external temperature, strain, and displacement. The refractive index of FBG has a constant relationship with the period of the grid. When the light passes through the FBG, the FBG will reflect the light that meets the Bragg phase matching condition, and the light that does not meet the condition will continue to transmit. When the temperature, strain, stress, or other physical quantities to be measured around the grating sensor change, it will cause the grating period or the core refractive index to change, thereby causing the Bragg wavelength shift. By measuring the offset of the Bragg center wavelength, the changes in the physical quantities of temperature and strain can be obtained. The principle is shown in Figure 1.

The FBG reflection wavelength λ_B that meets the Bragg phase matching condition can be expressed as

$$\lambda_B = 2n_{\text{eff}}\Lambda, \quad (1)$$

where n_{eff} is the effective refractive index of the optical fiber and Λ is the grid period of the FBG.

From the above formula, the change in Bragg reflection wavelength can be further expressed as

$$\Delta\lambda_B = 2\Delta n_{\text{eff}}\Lambda + 2n_{\text{eff}}\Delta\Lambda. \quad (2)$$

Obviously, the reflection wavelength λ_B of FBG is related to the effective refractive index and grid period of the optical fiber. When the external quantities (such as temperature and strain) change, the reflection wavelength of FBG used for measurement will drift. Therefore, by detecting the change of the reflection wavelength of FBG, the external quantities can be measured.

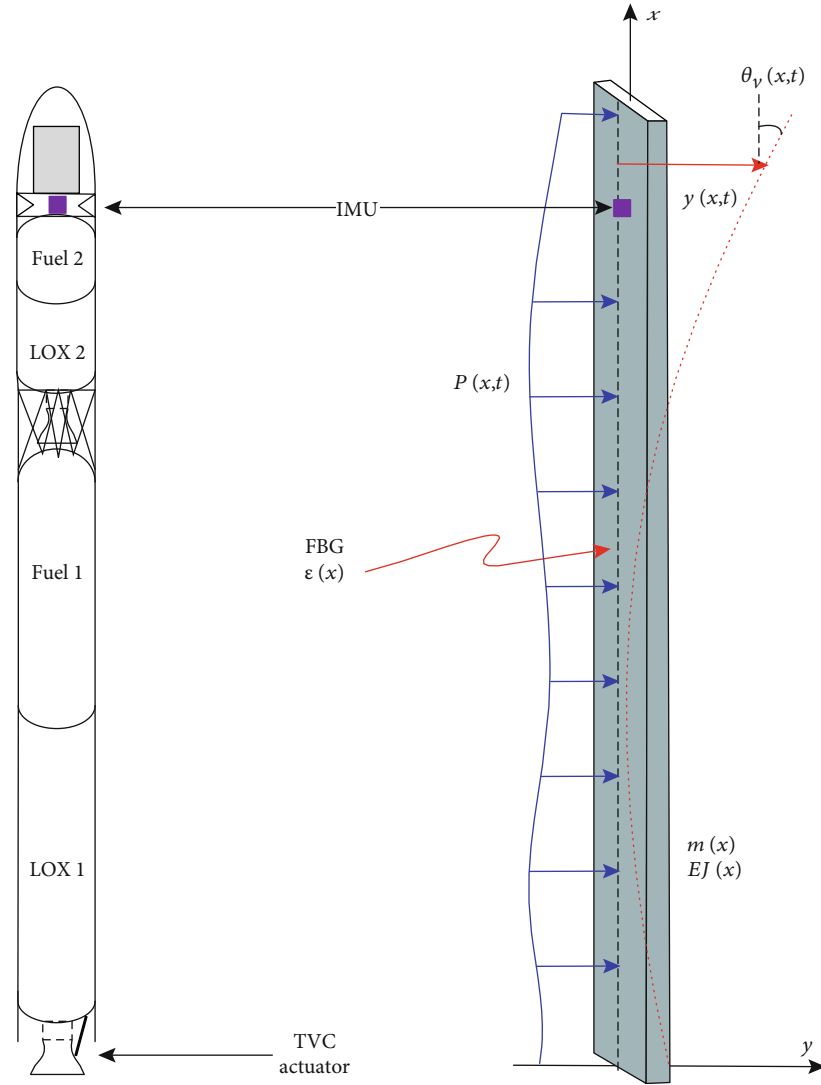


FIGURE 2: Beam representation of a flexible rocket.

Assuming the temperature keeps constant, the grating period is proportional to the strain induced by axial uniform stress:

$$\varepsilon = \frac{\Delta\Lambda}{\Lambda}. \quad (3)$$

At the same time, strain also changes the density of FBG, which further changes the effective refractive index n_{eff} . The relationship between the effective refractive index change and the strain is

$$\Delta n_{\text{eff}} = \frac{n_{\text{eff}}^3}{2} (v(p_{11} + p_{12}) - p_{12})\varepsilon, \quad (4)$$

where v is Poisson's ratio of the fiber and p_{11} and p_{12} are the photoelastic coefficients of the fiber. To simplify the formula,

a variable called FBG photoelastic coefficient is introduced:

$$p_e = \left(\frac{n_{\text{eff}}^2}{2} \right) [p_{12} - v(p_{11} + p_{12})], \quad (5)$$

$$\varepsilon = \frac{1}{(1 - p_e)} \frac{\Delta\lambda_B}{\lambda_B}.$$

The Bragg wavelength change is proportional to the external stress (for single-mode SiO₂ fiber, $p_e = 0.22$).

Measurement errors exist due to the imperfect packaging of FBG, transmission efficiency, and ambient temperature, which can be expressed as

$$e = \left| \frac{\varepsilon - \varepsilon_s}{\varepsilon} \right|. \quad (6)$$

At present, the strain measurement error of the corrected strain optical fiber sensor can be reduced to less than 5% [15].

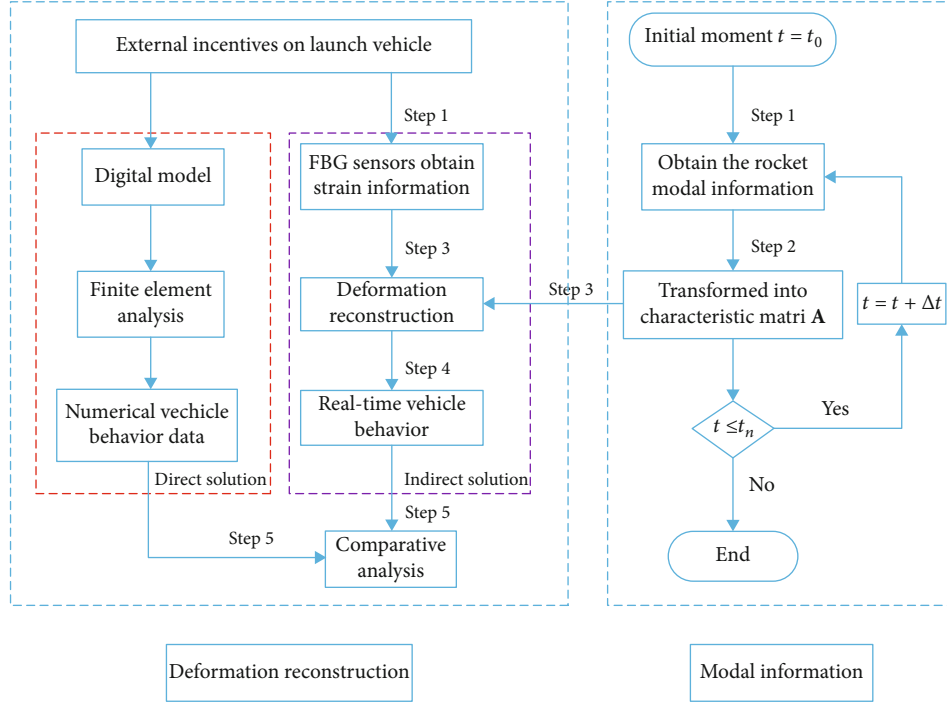


FIGURE 3: Flowchart of the deformation reconstruction method.

2.2. *Euler–Bernoulli Beam Model.* As shown in Figure 2, a flexible rocket can be simplified as a nonuniform free-free Euler–Bernoulli beam. The elastic vibrations can be described by the following differential equations:

$$\frac{\partial^2}{\partial x^2} \left(EJ(x) \frac{\partial^2 y(x, t)}{\partial x^2} \right) + m(x) \frac{\partial^2 y(x, t)}{\partial t^2} = P(x, t), \quad (7)$$

where $y(x, t)$ is the lateral displacement of the beam model relative to the x -axis, $m(x)$ is the mass distribution function of the rocket, $EJ(x)$ is the bending stiffness, and $P(x, t)$ is the transverse force on a unit length of the beam. The free-beam boundary condition requires the following relations to be satisfied:

$$\begin{aligned} EJ(0)y''(0) &= 0, & EJ(L)y''(L) &= 0, \\ (EJ(0)y''(0))' &= 0, & (EJ(L)y''(L))' &= 0. \end{aligned} \quad (8)$$

In the study of elastic vibrations of a flexible rocket, the deformation is considered to be a linear combination of the linear normal modes, given as

$$y(x, t) = \sum_{j=1}^{\infty} \varphi_j(x) \eta_j(t), \quad (9)$$

where $\varphi_j(x)$ is the j -th mode shape and $\eta_j(t)$ is the time-dependent amplitude of the j -th mode. $\varphi_j(x)$ can be determined by the finite element method. For a beam vibration

system, the finite element model of the Euler–Bernoulli beams is given as follows:

$$\mathbf{M}\ddot{\mathbf{X}}(t) + \mathbf{C}\dot{\mathbf{X}}(t) + \mathbf{K}\mathbf{X}(t) = \mathbf{F}(t), \quad (10)$$

where \mathbf{M} , \mathbf{C} , and \mathbf{K} are the inertia matrix, damping matrix, and stiffness matrix, respectively; $\mathbf{X}(t)$, $\dot{\mathbf{X}}(t)$, and $\ddot{\mathbf{X}}(t)$ are the displacement, speed, and acceleration of the system, respectively; and $\mathbf{F}(t)$ is the excitation force vector.

2.3. *Deformation Reconstruction of a Flexible Rocket.* There are no analytical functions for the vibration modes of the variable mass nonuniform beam model, and the discrete mode points need to be fitted by a continuous function [12]. Legendre polynomials are a set of complete and orthogonal polynomials defined in the domain of $[-1, 1]$, which can be used to fit a group of discrete mode solutions derived from Equation (10). The general equations for the shifted Legendre polynomials are given as follows:

$$\begin{aligned} P_0(x) &= 1, & P_1(x) &= 2x - 1, \\ P_{i+1}(x) &= \frac{(2i+1)(2x-1)P_i(x) - iP_{i-1}(x)}{i+1}. \end{aligned} \quad (11)$$

The mode shape $\varphi_j(x)$ can be fitted by the linear combination of $(m+1)$ Legendre polynomials as follows:

$$\varphi_j = \sum_{i=0}^{\infty} a_{ij} P_i(x) \approx a_{0j} P_0(x) + a_{1j} P_1(x) + \dots + a_{mj} P_m(x), \quad (12)$$

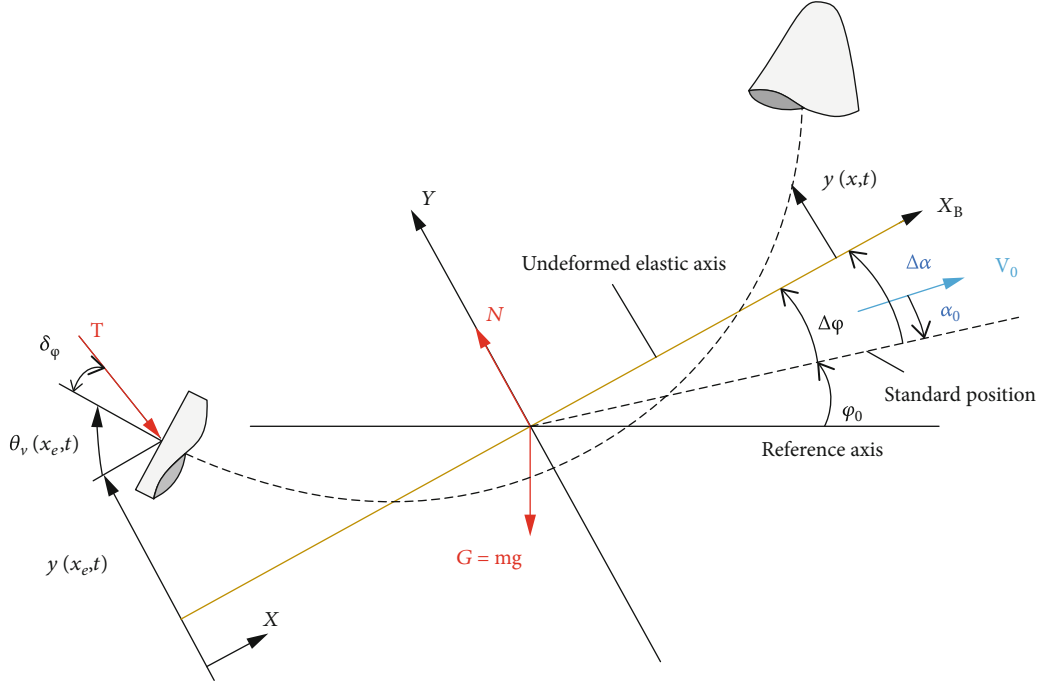


FIGURE 4: Disturbance coefficient of an elastic rocket in the pitch plane.

where a_{ij} is the Legendre polynomial coefficient. For the first n -order modes, the approximate values can be fitted by the linear combinations of the first $m + 1$ shifted Legendre polynomials as follows:

$$\begin{aligned} \Phi(\mathbf{x}) &= [\varphi_1 \quad \varphi_2 \quad \cdots \quad \varphi_n] \\ &= [P_0(x) \quad P_1(x) \quad P_2(x) \quad \cdots \quad P_m(x)] \\ &\quad \cdot \begin{bmatrix} a_{01} & a_{02} & \cdots & a_{0n} \\ a_{11} & a_{12} & \cdots & a_{1n} \\ a_{21} & a_{22} & \cdots & a_{2n} \\ \vdots & \vdots & \cdots & \vdots \\ a_{m1} & a_{m2} & \cdots & a_{mn} \end{bmatrix} = \mathbf{P}(\mathbf{x})\mathbf{A}. \end{aligned} \quad (13)$$

The characteristic coefficient matrix \mathbf{A} is obtained by the following formula:

$$\mathbf{A} = \mathbf{P}(\mathbf{x})^{-1} \Phi(\mathbf{x}). \quad (14)$$

Once the characteristic coefficient matrix \mathbf{A} of the model is determined, the mode shapes of the nodal rotations can be obtained by taking the derivative of $\mathbf{P}(\mathbf{x})$ as follows:

$$\Phi_{\theta}(\mathbf{x}) = [\varphi_{1\theta} \quad \varphi_{2\theta} \quad \cdots \quad \varphi_{n\theta}] = \mathbf{P}'(\mathbf{x})\mathbf{A}. \quad (15)$$

According to the kinematics, the tensile strain due to the beam bending (ε) is related to the nodal displacement (y) as follows:

$$\varepsilon(x, t) = -z_0 y''(x, t), \quad (16)$$

where z_0 is the distance from the reference line of the beam (in this study, the center axis of the beam is taken as the baseline) to the position of the FBG sensor, which is usually arranged on the surface of the beam to measure the strain. When $\varepsilon(x, t)$ is measured by FBG sensors, the instantaneous modal coordinates $\eta(t)$ can be solved by the following formula:

$$\varepsilon(x, t) = -z_0 \mathbf{P}''(\mathbf{x}) \mathbf{A} \eta(t). \quad (17)$$

When the instantaneous mode coordinate $\eta(t)$ is known, the deformation displacement at each point of the beam can be obtained by the polynomial $P(x)$ and characteristic coefficient matrix \mathbf{A} . The velocity at each point of the beam can be obtained by the following backward finite difference equations:

$$\begin{aligned} y(x, t) &= \mathbf{P}(\mathbf{x}) \mathbf{A} \eta(t), \\ v(x, t) &= \mathbf{P}(\mathbf{x}) \mathbf{A} \dot{\eta}(t) = \frac{1}{\Delta t} \mathbf{P}(\mathbf{x}) \mathbf{A} (\eta_t - \eta_{t-\Delta t}). \end{aligned} \quad (18)$$

By inserting the Legendre polynomials $P(x)$ into Equation (18), the beam deflection angle θ_v and angular velocity $\dot{\theta}_v$ caused by vibration can be obtained as follows:

$$\begin{aligned} \theta_v(x, t) &= \mathbf{P}'(\mathbf{x}) \mathbf{A} \eta(t), \\ \dot{\theta}_v(x, t) &= \mathbf{P}'(\mathbf{x}) \mathbf{A} \dot{\eta}(t). \end{aligned} \quad (19)$$

However, there may be a variety of errors in the fitting process, resulting in a deviation between the reconstructed

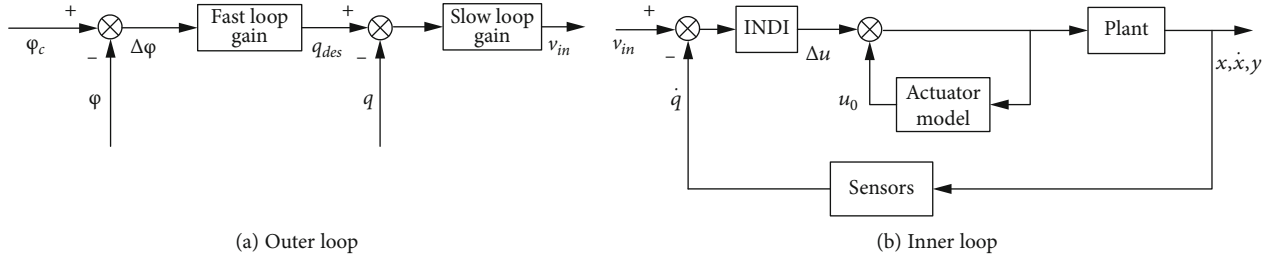


FIGURE 5: Control block diagram of the (a) outer loop and (b) inner loop.

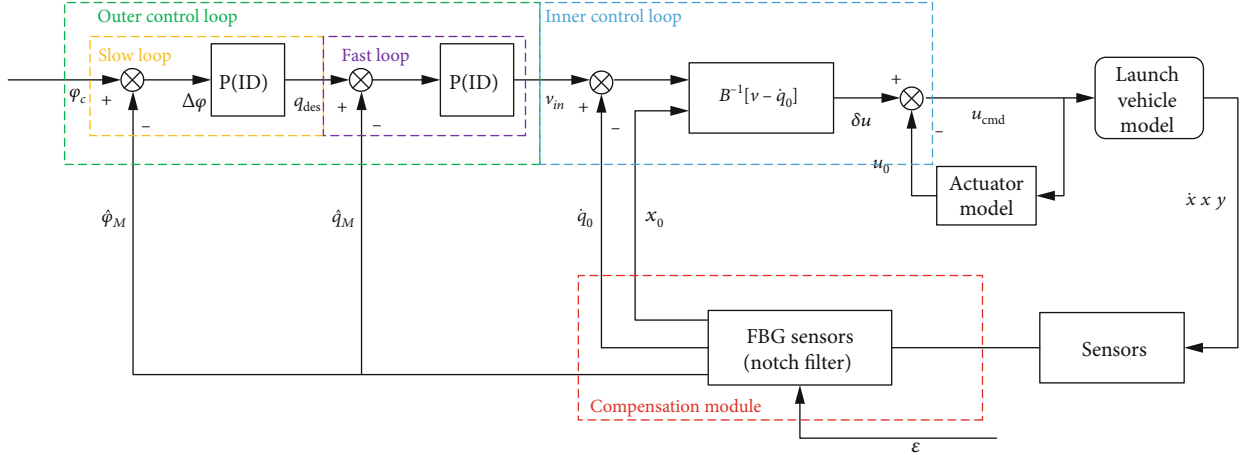


FIGURE 6: Block diagram of incremental dynamic inversion control based on deformation compensation.

TABLE 1: Model parameters.

Property	Value	Unit
Span, L	1.000	m
Cross-section thickness, b	0.006	m
Cross-section width, h	0.021	m
Material density, ρ	2667	kg/m ³
Young's modules, E	63.5	GPa

deformation and the actual state. The reconstruction error e_v is defined as

$$e_v = \left| \frac{\widehat{\kappa} - \kappa}{\kappa} \right|, \quad (20)$$

where $\widehat{\kappa}$ represents the state information of the rocket vibration obtained by shape reconstruction, including displacement, velocity, angle, and angular velocity. κ represents the actual status information.

In summary, the procedure of the deformation reconstruction method of a flexible rocket is as follows.

Step 1. Set the simulation time interval $[t_1, t_2]$ and the simulation step size Δt . Acquire the modal change information of the rocket beam model in this time period via a ground vibration test or finite element simulation. Obtain a set of strain values ε measured at time t using the FBG sensor array.

Step 2. Fit the modal information at this time with a continuous Legendre polynomial to obtain the characteristic coefficient matrix \mathbf{A} for this time point.

Step 3. Introduce the strain value ε and the characteristic coefficient matrix \mathbf{A} into Equation (17), to solve the instantaneous modal amplitude $\eta(t)$.

Step 4. Substitute $\eta(t)$ into Equations (18) and (19) to obtain the displacement, deflection angles, and angular velocities of the beam model.

Step 5. Compare the deformation information of the launch vehicle obtained by the deformation reconstruction method (indirect solution) and the finite element method (direct solution), and assess the accuracy of the launch vehicle body reconstruction method.

The deformation fitting process based on the FBG sensor is shown in Figure 3.

3. High-Precision Attitude Control Method of a Rocket Based on Deformation Reconstruction

3.1. Dynamic Modeling of Attitude and Vibration of a Launch Vehicle. The pitching plane vibrations of the launch vehicle are the key for system design and flight control. In this paper,

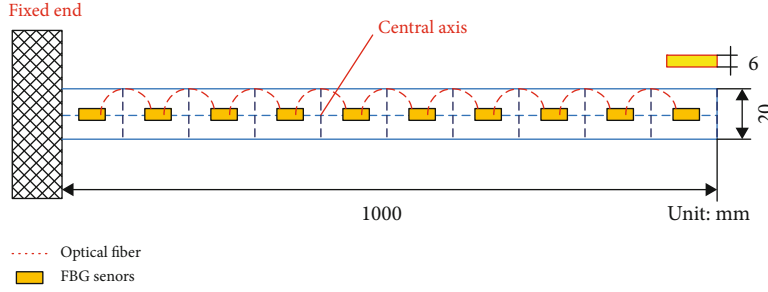


FIGURE 7: Beam element model and location of measurement points.

the pitching plane vibrations and deformation are mainly modeled. The model used in this paper is shown in Figure 4. The nominal trajectory of the system is planned to keep the launch vehicle position close to a zero angle of attack. For equilibrium conditions, the assumption that the angle of attack is close to zero is quite valid, and any change in the angle of attack can be considered to be a disturbance from the equilibrium conditions. Therefore, considering a small disturbance, the linearized dynamic equations of the pitch channel of the launch vehicle considering elastic vibrations are as follows [16]:

$$\begin{cases} \Delta\dot{\theta} = c_1\Delta\alpha + c_2\Delta\theta + c_3\delta_\varphi + c_3'\ddot{\delta}_\varphi + \sum_{i=1}^n c_{1i}\dot{\eta}_i + \sum_{i=1}^n c_{2i}\eta_i + \bar{F}_{byc}, \\ \Delta\ddot{\varphi} + b_1\Delta\dot{\varphi} + b_2\Delta\alpha + b_3\delta_\varphi + b_3''\ddot{\delta}_\varphi + \sum_{i=1}^n b_{1i}\dot{\eta}_i + \sum_{i=1}^n b_{2i}\eta_i = \bar{M}_{bz}, \\ \Delta\theta = \Delta\varphi - \Delta\alpha, \\ \ddot{\eta}_i + 2\xi_i\omega_i\dot{\eta}_i + \omega_i^2\eta_i = D_{1i}\Delta\dot{\varphi} + D_{2i}\Delta\alpha + D_{3i}\delta_\varphi + D_{3i}'\ddot{\delta}_\varphi - Q_{iy}, \end{cases} \quad (21)$$

where n is the number of bending modes, $\Delta\alpha$ is the angle of attack, $\Delta\theta$ is the flight path angle, $\Delta\varphi$ is the direction of the vehicle axis, δ_φ is the Gimbal deflection angle, η_i is the generalized coordinate of the vibration modes, \bar{F}_{byc} , \bar{M}_{bz} , and Q_{iy} are the perturbed force, torque, and generalized disturbance force coefficients, respectively, ω_i and ξ_i are the bending mode natural frequency and damping ratio, respectively, and c_1 , c_2 , c_3 , c_3' , c_{1i} , c_{2i} , b_1 , b_2 , b_3 , b_3'' , b_{1i} , b_{2i} , D_{1i} , D_{2i} , D_{3i} , and D_{3i}' are coefficients of the pitching dynamics.

The system state equation of the pitch channel is given as follows:

$$\dot{\mathbf{x}} = \mathbf{A}_p\mathbf{x} + \mathbf{B}_p\mathbf{u} + \mathbf{D}_p, \quad (22)$$

where \mathbf{A}_p , \mathbf{B}_p , and \mathbf{D}_p are the system, control, and disturbance matrices, respectively.

To simplify the analysis, the interference term \mathbf{D}_p is ignored in the design process, and the values of the n bending

modes are set to 1. The corresponding state space matrix can be written as follows:

$$\mathbf{A}_p = \begin{pmatrix} c_2 - c_1 & c_1 & 0 & c_{21} & c_{11} \\ 0 & 0 & 1 & 0 & 0 \\ b_2 & -b_2 & -b_1 & -b_{21} & -b_{11} \\ 0 & 0 & 0 & 0 & 1 \\ -D_{21} & D_{21} & D_{11} & -\omega_1^2 & -2\xi_1\omega_1 \end{pmatrix}, \quad (23)$$

$$\mathbf{B}_p = \begin{pmatrix} c_3 \\ 0 \\ -b_3 \\ 0 \\ D_{31} \end{pmatrix},$$

where the state vector $x = [\theta, \varphi, q, \eta, \dot{\eta}]^T$. Since the control command is the deflection angle of the gimbals, $u = \delta_\varphi$. According to Equation (2), the deformation at any point of the launch vehicle can be approximately regarded as a combination of the linear superposition of various modes. The deflection angle $\theta(x, t)$ caused by the vibration is given by the following formula:

$$\theta(x, t) = \sum_{i=1}^N w_i(x)\eta_i(t), \quad (24)$$

where $w_i(x) = d\varphi_i(x)/dx$. The measured pitch angle and pitch angle rate are expressed as follows:

$$\begin{aligned} \varphi_M &= \varphi + \theta(x_{gyro}, t), \\ q_M &= q + \dot{\theta}(x_{gyro}, t), \end{aligned} \quad (25)$$

where φ_M and q_M are the actual measured pitch angle and pitch angle rate, respectively, and x_{gyro} is the position of the attitude sensor.

3.2. Design of the High-Precision Attitude Control System

3.2.1. Incremental Dynamic Inverse Control Law. The incremental dynamic inversion control law is a nonlinear robust

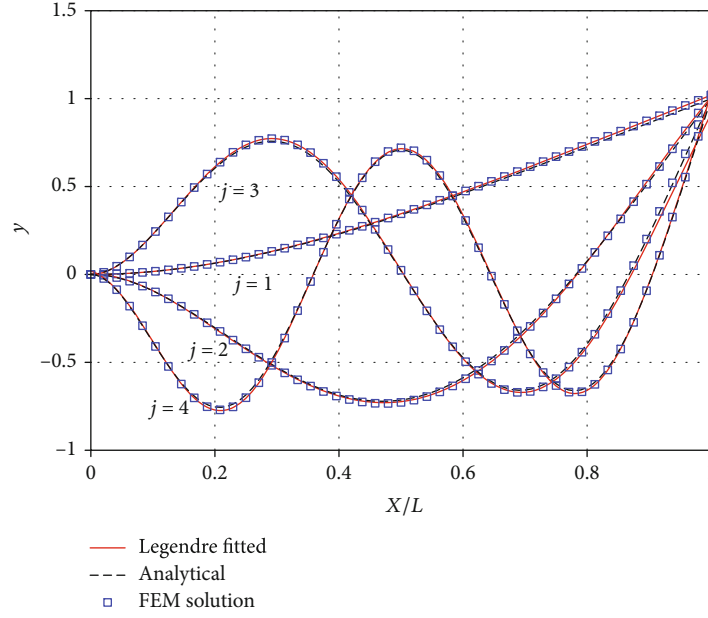


FIGURE 8: Analytical and finite element solutions for the first four modes of a cantilever beam and the fitted continuous mode shapes.

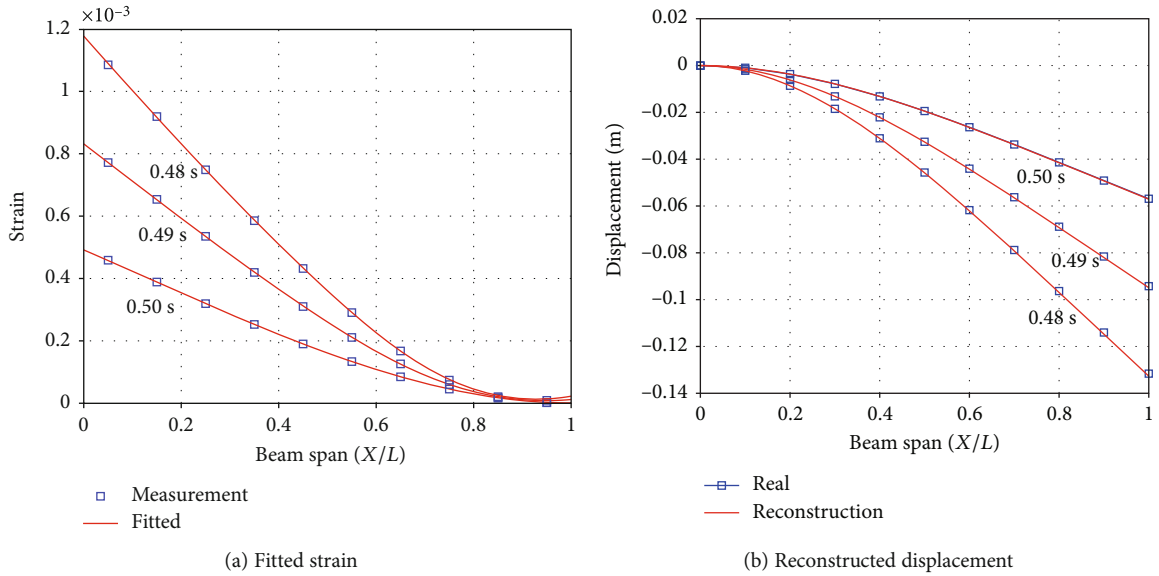


FIGURE 9: Fitted strain and reconstructed displacement at 0.5, 0.49, and 0.48 s.

control method that is insensitive to model parameters. The method uses angular acceleration feedback [17]. The control of a nonlinear system is assumed to be affine:

$$\begin{cases} \dot{\mathbf{x}} = \mathbf{f}(\mathbf{x}) + \mathbf{G}(\mathbf{x}, \mathbf{u}), \\ \mathbf{y} = \mathbf{h}(\mathbf{x}), \end{cases} \quad (26)$$

where \mathbf{x} is the n -dimensional state quantity, \mathbf{u} is the $m \times 1$ control input, $\mathbf{f}(\mathbf{x})$ represents the system dynamics, $\mathbf{G}(\mathbf{x}, \mathbf{u})$ is an $(n \times m)$ -dimensional state-dependent control matrix, and \mathbf{y} is a p -dimensional output. To obtain the approximate

dynamics in incremental form, the first-order Taylor series expansion of $\dot{\mathbf{x}}$ about (x_0, u_0) is

$$\begin{aligned} \dot{\mathbf{x}} \approx & \mathbf{f}(\mathbf{x}_0) + \mathbf{G}(\mathbf{x}_0, \mathbf{u}_0) + \frac{\partial}{\partial \mathbf{x}} (\mathbf{f}(\mathbf{x}) + \mathbf{G}(\mathbf{x}, \mathbf{u}))_{\mathbf{x}_0, \mathbf{u}_0} (\mathbf{x} - \mathbf{x}_0) \\ & + \frac{\partial}{\partial \mathbf{u}} \mathbf{G}(\mathbf{x}, \mathbf{u})_{\mathbf{x}_0, \mathbf{u}_0} (\mathbf{u} - \mathbf{u}_0). \end{aligned} \quad (27)$$

The equation of state at the point (x_0, u_0) is

$$\dot{\mathbf{x}}_0 = \mathbf{f}(\mathbf{x}_0) + \mathbf{G}(\mathbf{x}_0, \mathbf{u}_0). \quad (28)$$

TABLE 2: Deformation fitting errors at different times.

Time	0.48 s	0.49 s	0.50 s
ERR	0.0246	0.0237	0.0211
RMSE	0.1246	0.1227	0.1176

Two partial derivatives are defined as follows:

$$\begin{cases} \bar{\mathbf{A}} = \frac{\partial}{\partial \mathbf{x}} (\mathbf{f}(\mathbf{x}) + \mathbf{G}(\mathbf{x}, \mathbf{u})), \\ \bar{\mathbf{B}} = \frac{\partial}{\partial \mathbf{u}} \mathbf{G}(\mathbf{x}, \mathbf{u}). \end{cases} \quad (29)$$

The output equation with respect to time can be obtained as follows:

$$\dot{\mathbf{y}} = \frac{\partial \mathbf{h}(\mathbf{x})}{\partial \mathbf{x}} \dot{\mathbf{x}} \approx \mathbf{h}_x (\dot{\mathbf{x}}_0 + \bar{\mathbf{A}}(\mathbf{x}_0, \mathbf{u}_0) \Delta \mathbf{x} + \bar{\mathbf{B}}(\mathbf{x}_0, \mathbf{u}_0) \Delta \mathbf{u}). \quad (30)$$

For a sufficiently high control update (and thus, a small time increment), \mathbf{x} approaches \mathbf{x}_0 . The increment $\Delta \mathbf{x}$ of the state variable is a high-order small quantity relative to the increment $\Delta \mathbf{u}$ of the control input, so it can be omitted. The expected closed-loop dynamic characteristic is \mathbf{v} . The incremental dynamic inverse control law is designed to make the system output dynamic characteristics track the expected characteristics, which is expressed as $\mathbf{v} = \dot{\mathbf{y}}$. By substituting this into Equation (20), the control input is written as follows:

$$\mathbf{u} = \mathbf{u}_0 + \Delta \mathbf{u} = \mathbf{u}_0 + (\mathbf{h}_x \bar{\mathbf{B}}(\mathbf{x}_0, \mathbf{u}_0))^{-1} (\mathbf{v} - \mathbf{h}_x \dot{\mathbf{x}}_0), \quad (31)$$

where \mathbf{u}_0 is a nominal (or reference) control.

The control law of the system is not dependent on the state of the system. The incremental control law algorithm requires the control system to use the derivatives of the state variables, so angular acceleration feedback is needed in the rocket attitude control.

3.2.2. Design of Control Law Based on Deformation Information Compensation. For the attitude control of the rocket studied in this paper, the dynamics equation of the rocket is shown in Equation (12). The state quantity is defined as $\mathbf{x} = [\theta, \varphi, q, \eta, \dot{\eta}]^T$, and the control input is \mathbf{u} . In the current configuration, \mathbf{u} is the swing nozzle rotation angle δ_φ . From Equation (31), the corresponding incremental dynamic inverse control law is obtained as follows:

$$\Delta \mathbf{u} = \mathbf{B}^{-1} (\mathbf{v} - \dot{\mathbf{q}}_0), \quad (32)$$

where $\dot{\mathbf{q}}_0$ is the angular acceleration in the pitching direction of the rocket at the current moment, and the inverse matrix of $\mathbf{h}_x \bar{\mathbf{B}}(\mathbf{x}_0, \mathbf{u}_0)$ is equal to \mathbf{B}^{-1} .

According to the characteristics of the rocket attitude control, a dual-loop control law is designed based on the incremental dynamic inverse control law. The outer loop includes the attitude angle loop (slow loop) and angular velocity loop (fast loop). The desired angular velocity of the

outer loop q_{des} can be obtained by a proportional-integral-derivative (PID) or more complex control law. In this analysis, a simple proportional control is used:

$$\mathbf{q}_{\text{des}} = \mathbf{K}_{s,\text{out}} \Delta \boldsymbol{\varphi}. \quad (33)$$

The desired angular acceleration can also be obtained from a proportion control law:

$$\mathbf{v} = \mathbf{K}_{q,\text{out}} \mathbf{q}_e = \mathbf{K}_{q,\text{out}} (\mathbf{q}_{\text{des}} - \mathbf{q}), \quad (34)$$

where $K_{s,\text{out}}$ and $K_{q,\text{out}}$ are the proportional gain coefficients of the slow loop and the fast loop, respectively. The inner loop is the angular acceleration loop, which adopts an incremental dynamic inverse control law:

$$\mathbf{u}_c = \mathbf{u}_0 + \Delta \mathbf{u} = \mathbf{u}_0 + \mathbf{B}^{-1} [\mathbf{v} - \dot{\mathbf{q}}_0]. \quad (35)$$

The control block diagrams of the inner and outer loops are shown in Figure 5, where \mathbf{u}_0 is the control input at the last sampling time, and the subscript c represents the instruction.

In the actual control process, the attitude angle and attitude angular rate (in the current study, these are the pitch angle and the pitch rate, respectively) obtained by the measuring device contain the elastic vibration information of the rocket body, which cannot provide accurate measurement information for the guidance, navigation, and control (GNC) system. When the vibration information of the rocket body is measured by an FBG sensor, the attitude angle and angular rate error caused by the rocket vibrations can be compensated for by the feedback loop, as shown in Figure 6.

According to Equation (18), the deflection of a flexible rocket can be estimated using an FBG sensor array. FBG measurements can be used to compensate for the pitch angle and pitch rate φ_M and q_M (the angular acceleration error caused by vibration is not considered in this paper):

$$\begin{cases} \hat{\varphi}_M = \varphi_M - \varphi_b, \\ \hat{q}_M = q_M - q_b, \end{cases} \quad (36)$$

where $\hat{\varphi}_M$ and \hat{q}_M are the pitch angle and pitch angle rate after compensation, respectively, and φ_b and q_b are the rocket vibration information obtained by the FBG measurement, which can be obtained using Equation (19).

4. Simulation Analysis

To verify the fitting accuracy of the reconfiguration algorithm of the flexible rocket and the feasibility of the incremental dynamic inversion control law based on FBG compensation, the above schemes were simulated, and the results are presented in this section.

4.1. Accuracy Analysis of Deformation Reconstruction. A Euler-Bernoulli cantilever beam is taken as the simulation object, and the model parameters are shown in Table 1. The beam was divided into ten elements. One FBG sensor was attached to the midpoint of each element, and all sensors

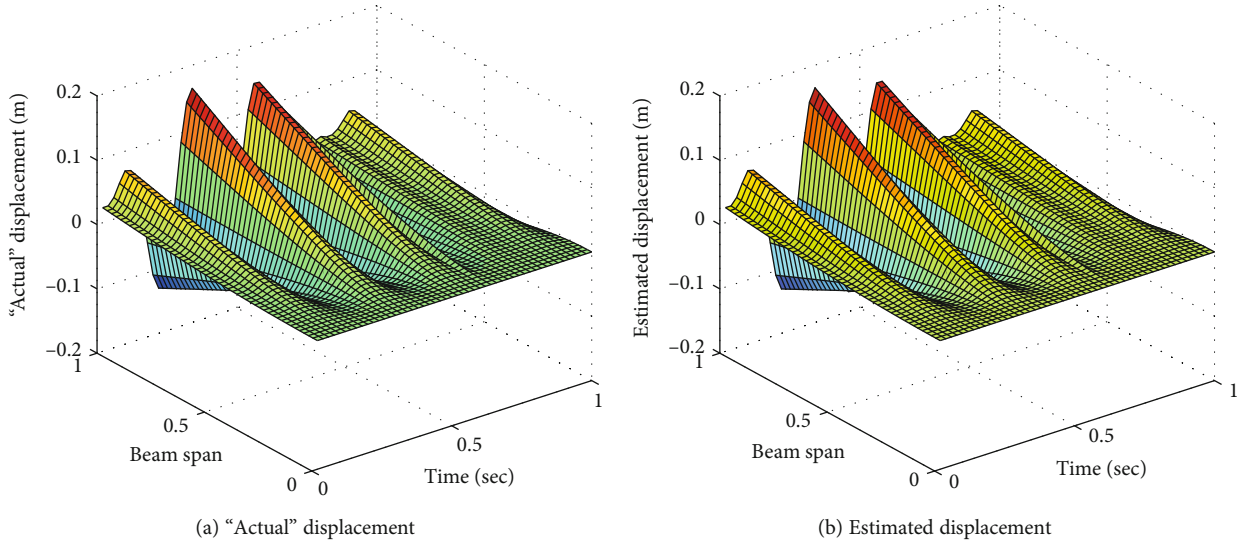
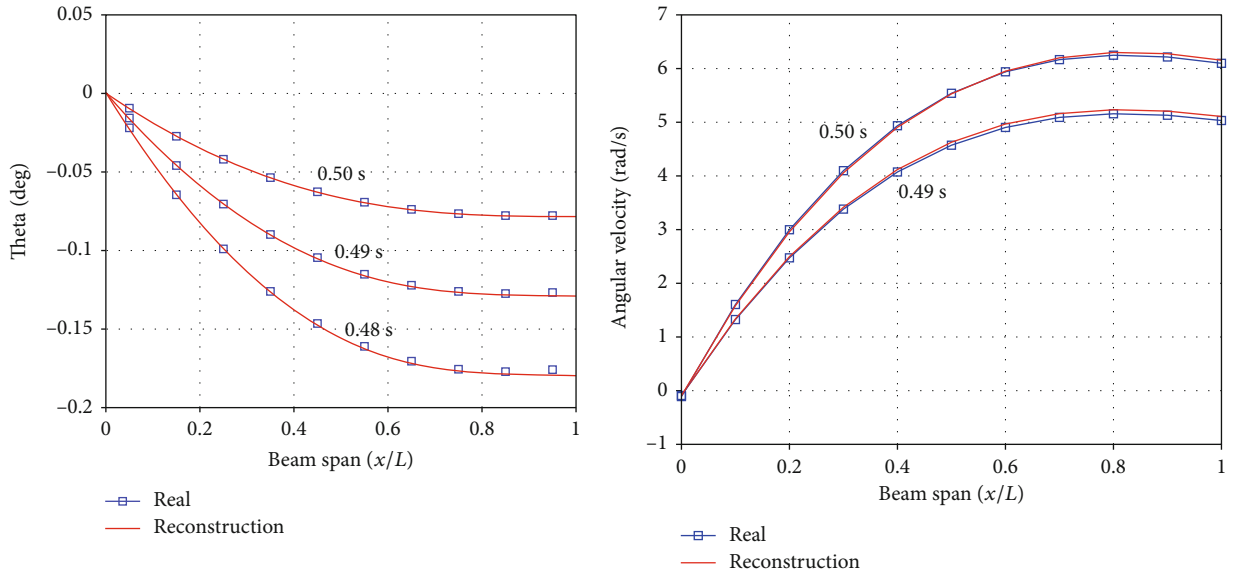


FIGURE 10: "Actual" and estimated displacement along the beam from 0 to 1 s.



(a) Reconstructed model angle at 0.5, 0.49, and 0.48 s (b) Reconstructed angular velocity at 0.49 and 0.5 s

FIGURE 11: Reconstructed angle and angular velocity of the equivalent model.

TABLE 3: Angle fitting errors.

Time	0.48 s	0.49 s	0.50 s
ERR	0.0273	0.0245	0.0183
RMSE	0.1128	0.1038	0.0887

were pasted along the center line of the beam surface at equal intervals. The strain values measured by ten FBG sensors attached to the surface of the beam were used to identify the displacement and velocity at each point of the beam. The node division and measuring point positions of the cantilever beam are shown in Figure 7. The vertical distance from the sensor to the beam reference

line was $b/2$. In theory, the input of the system should be the measurement data of an optical fiber sensor. In the current research, the transient response of the beam model was used as "measurement" data.

The boundary conditions used in the current study are described briefly. Cantilever boundary conditions were applied at the root of the rocket in the simulation cases in this section. Although this is not the case in actual rocket flight, the purpose of this section study is to explore and simulate the concept of using FBG sensors to track the lateral bending vibration of a flexible rocket, which can be easily excited and simulated under cantilever boundary conditions and tip loading. In addition, the method developed in this paper for analyzing the deformed structure of the rocket does not

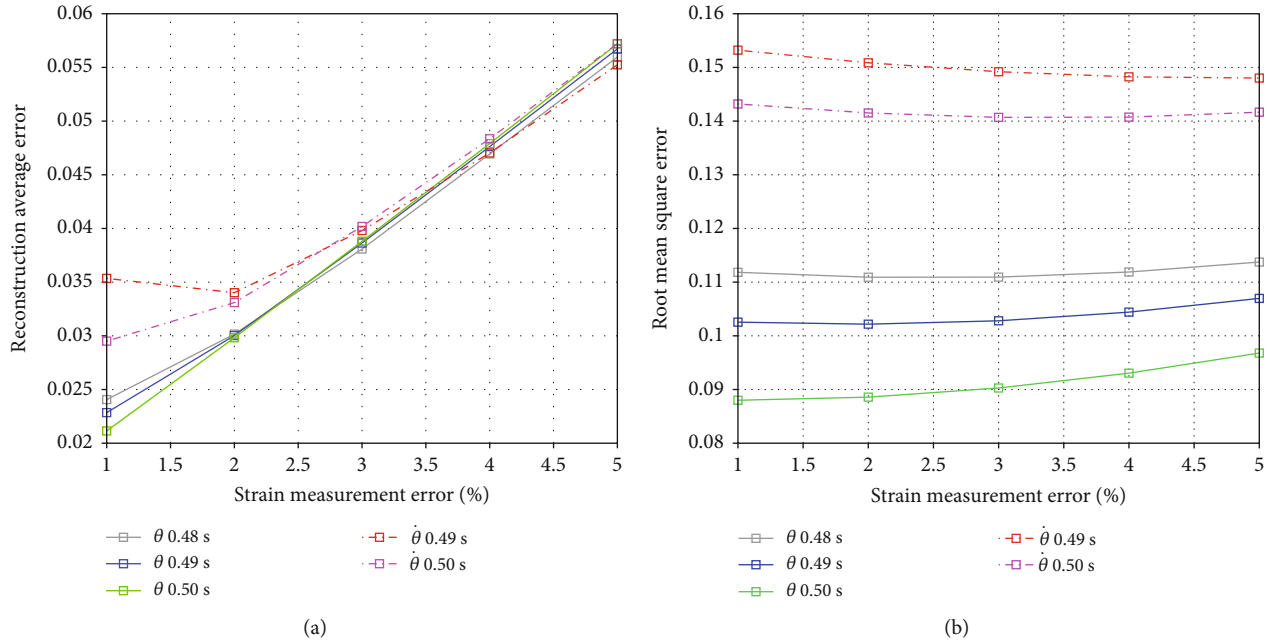


FIGURE 12: Reconstruction error varies with strain measurement error at 0.5, 0.49, and 0.48 s.

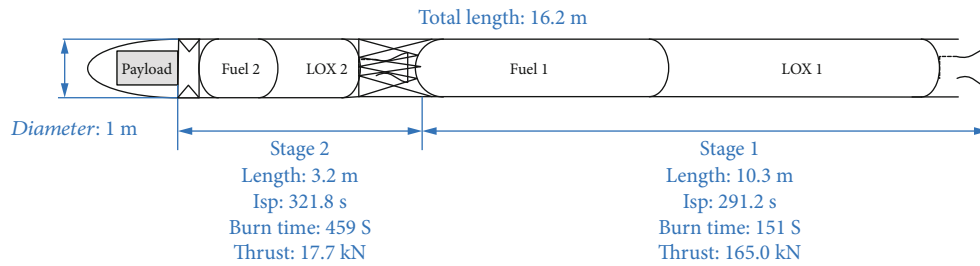


FIGURE 13: Geometry configuration of the miniature launcher.

exclude the free-flight condition of the rocket and can be applied in rocket ground vibration tests.

The first four mode curves fitted by Legendre polynomials are shown in Figure 8. The black dotted line in the figure represents the vibration mode of a cantilever beam with a single degree of freedom obtained using the vibration theory of continuous beams, and the blue boxes represent the discrete modal data obtained by the finite element analysis software, where the eigencoefficient matrix of the cantilever model was calculated.

When the characteristic coefficient matrix \mathbf{A} is known, the vibration displacement of the beam model under an external load can be reduced according to the strain data “measured” by the FBG. A sine load $F = 3 \sin(10\pi t)N$ was applied at the middle point of the top of the cantilever beam, and the instantaneous response of the beam model was obtained through the finite element software calculations. The transverse strain values of the beam at 0.5, 0.49, and 0.48 s were used for deformation fitting calculations. The fitting effect is shown in Figure 9(a).

To evaluate the fitting effect and quantify the deformation reconstruction error, the average error (ERR) and root

mean square error (RMSE) were used to describe the fitting error [12]:

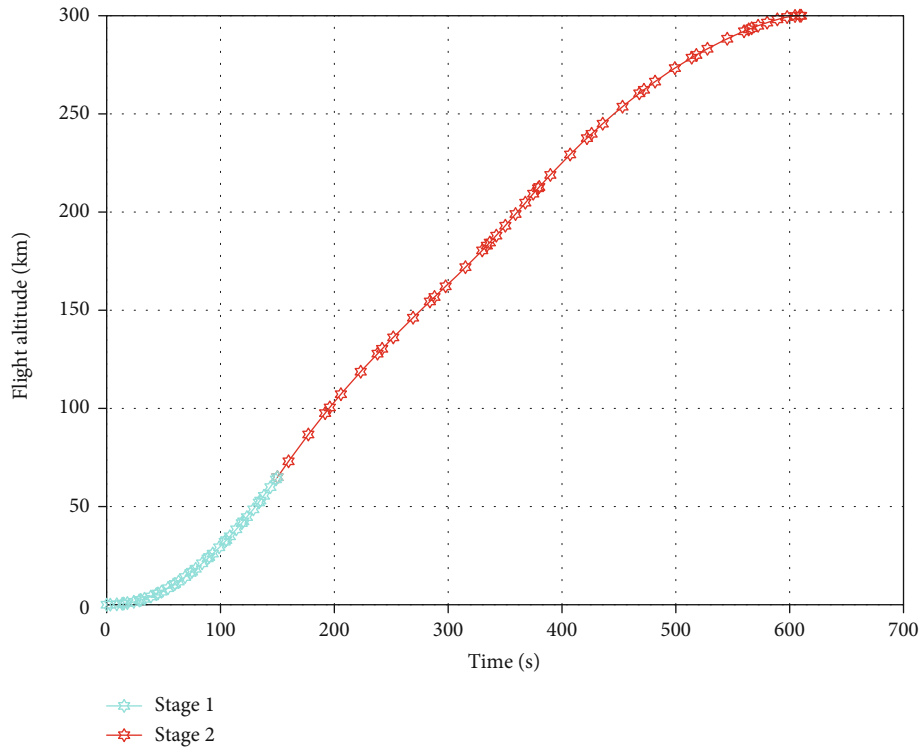
$$\text{ERR} = \frac{1}{N} \sqrt{\sum_{i=1}^N \left(\frac{Y_i - Y\wedge_i}{Y_i} \right)^2}, \quad (37)$$

$$\text{RMSE} = \sqrt{\frac{\sum_{i=1}^N (Y_i - Y\wedge_i)^2}{N - 1}},$$

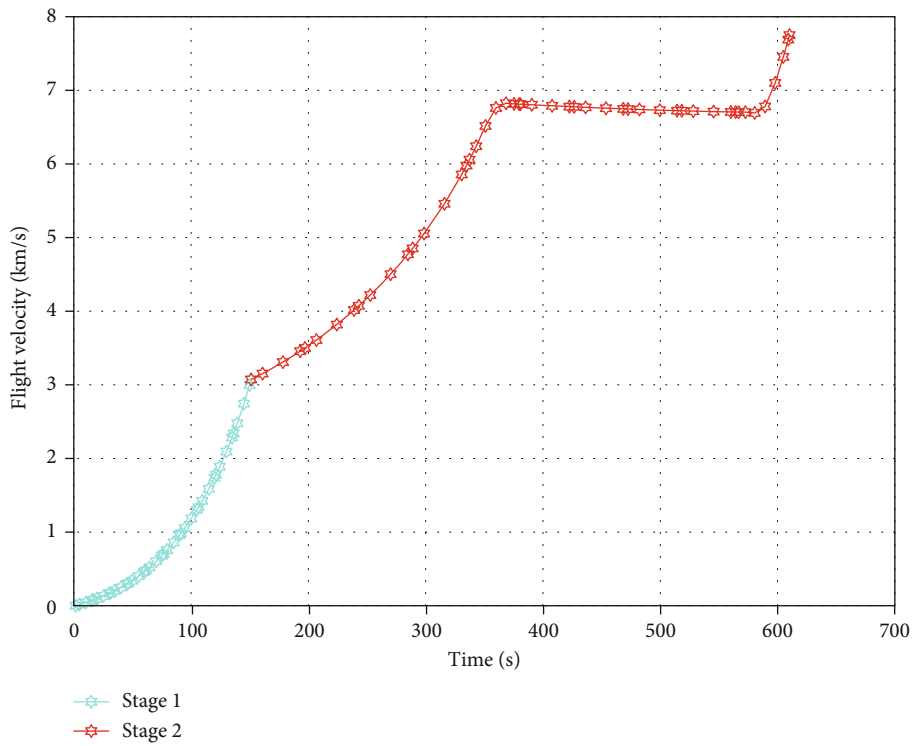
where Y_i is the simulated real lateral displacement of the beam structure, \hat{Y}_i is the displacement identified by the algorithm, and N is the total number of samples.

As shown in Figure 9(b), at 0.5, 0.49, and 0.48 s, the “real” and reconstructed values agreed closely. As shown in Table 2, the recognition error based on the Legendre polynomial algorithm was small and had a good fitting effect.

The previous indirect solutions were all carried out at 0.5, 0.49, and 0.48 s. To test the universality of the solution algorithm, the solution process was repeated in the range of 0 to 1 s. As shown in Figure 10, the values of the

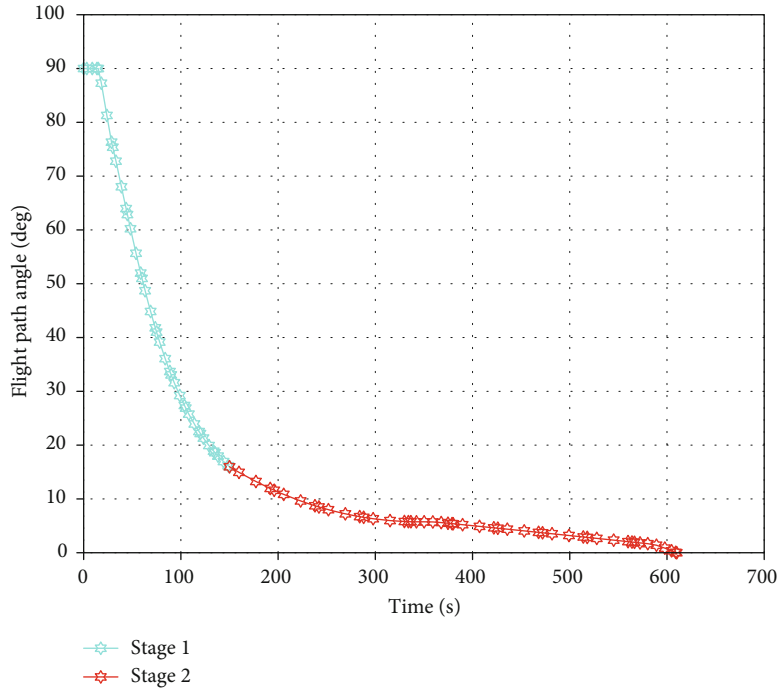


(a) Altitude

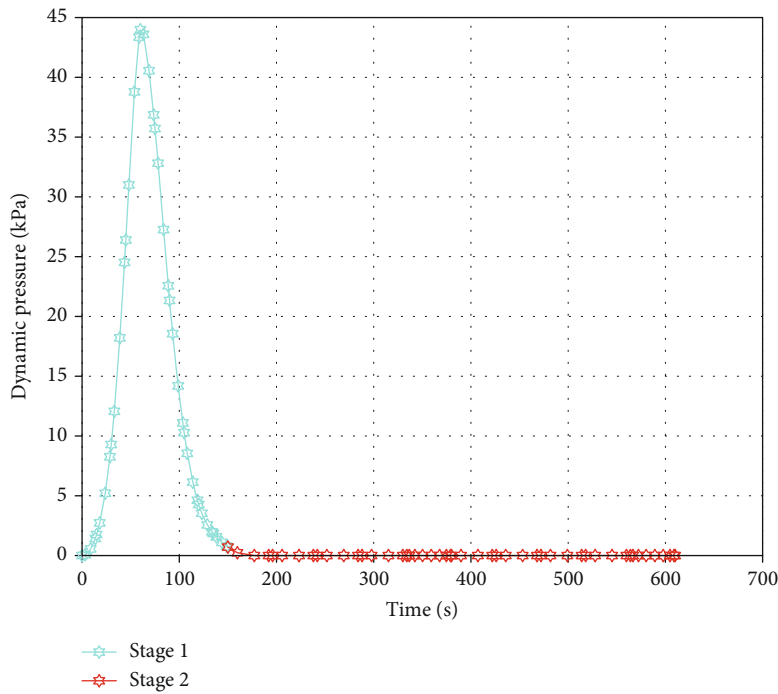


(b) Velocity

FIGURE 14: Continued.



(c) Flight path angle



(d) Dynamic pressure

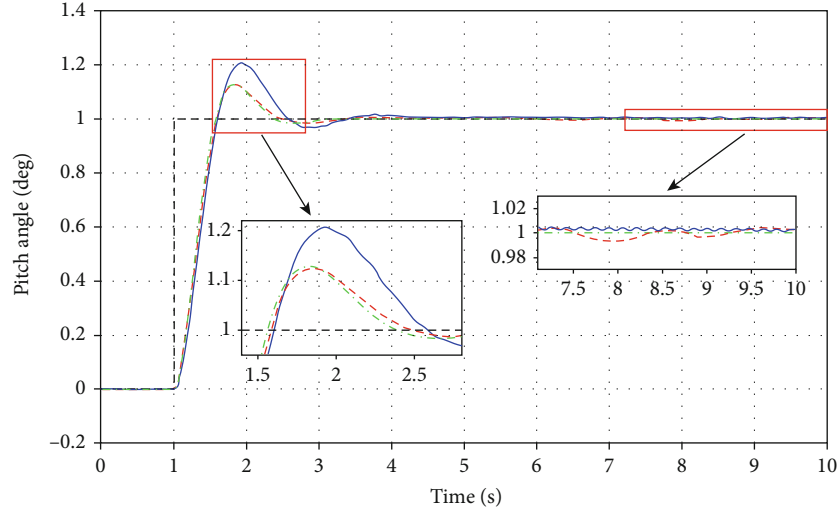
FIGURE 14: Trajectory performance of the miniature launcher.

TABLE 4: Performance results.

	Unit	Rigid	FBG compensation	Notch filter
$\sum \varphi_{err}$	°s	0.363	0.384	0.492
$\sum \delta$	°s	1.69	1.72	2.68

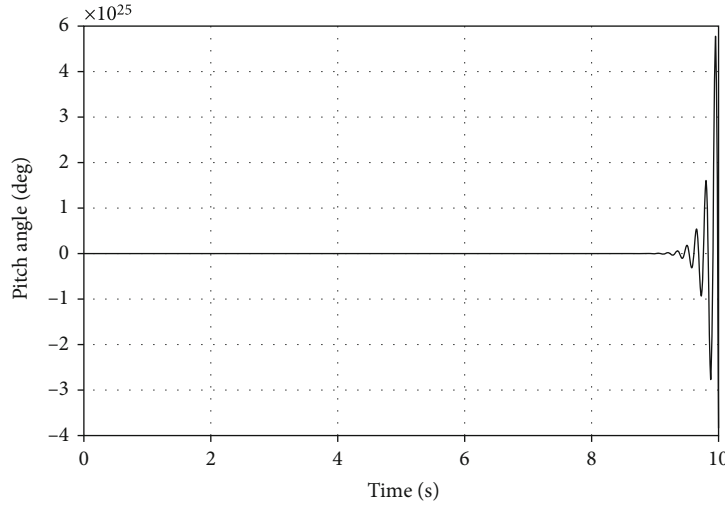
indirect solutions were almost the same as those of the direct solutions over the whole simulation time range, which indicated that the fitting accuracy of the algorithm was maintained well.

In the control system, it is necessary to compensate for the attitude angle and the attitude angular velocity and to process the displacement data according to Equation (19) to obtain the angle and angular velocity at each point of the



--- Command
 Flexible+notch filter
 Flexible+FBG
 Rigid

(a) Notch filter, FBG compensation, and rigidity



(b) Flexible model without compensation

FIGURE 15: Pitch angle response curves.

beam model. The strain data acquired at 0.5, 0.49, and 0.48 s were selected to estimate the angle along the transverse normal direction of the beam at 0.5, 0.49, and 0.48 s and the angular velocity at 0.5 and 0.49 s.

As shown in Figure 11 and Table 3, the angle fitting errors at 0.5, 0.49, and 0.48 s were small, and a good fitting effect was achieved. In addition, the backward difference method could basically restore the angular velocity variations along the transverse normal direction of the beam. The average errors of the angular velocity at 0.5 and 0.49 s were 3.4% and 3.7%, respectively. Farther from the fixed end, the relative error was greater. The possible reasons for this include the following: there were errors in the calculation of the initial coefficient matrix A , which caused the error to be amplified in the backward difference process, and the selection of the backward finite difference step size affected the calculation accuracy.

Figure 12 shows the relationship between the reconstruction error and the strain measurement error. Three sampling points were selected, which are 0.48 s, 0.49 s, and 0.50 s. It can be seen that when the strain measurement error changes within the range of 1~5%, the average error of the reconstructed angle θ and angular velocity $\dot{\theta}$ change near linearly, and their root mean square error remains nearly constant.

4.2. Simulation and Analysis of Attitude Control Performance. At present, there is little accessible data about launch vehicles with a large slenderness ratio. Therefore, a conceptually designed launch vehicle is adopted for control performance simulation which has a slenderness ratio as high as 16.2. Its payload capacity is 100 kg (300 km circular SSO). Both stages use LOX/RP-1 as a propellant. The propellant tanks are common bulkhead Al-Li alloy tanks, and the thickness is 4 mm (the schematic diagram of the launch vehicle is

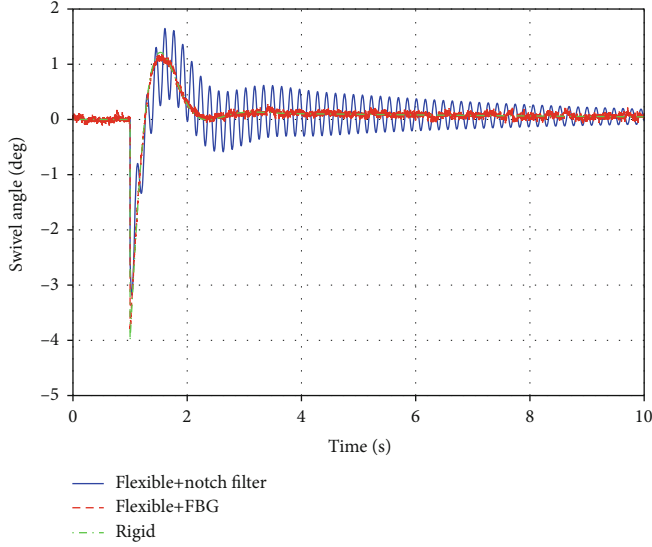


FIGURE 16: Swivel angle curve.

shown in Figure 13, and the detailed parameters are listed in Tables 6 and 7 which are presented in Appendix A).

Figures 14(a) and 14(b) show the altitude and velocity history of the miniature launcher. Figures 14(c) and 14(d) show the flight path angle and dynamic pressure with time. The peak dynamic pressure is located at 60.2 s (10.57 km), about 44.1 kPa. At maximum dynamic pressure, the launcher mass is 8072 kg, the velocity is 490.3 m/s, and the flight path angle is 44.2°. The system matrix and control matrix at maximum dynamic pressure are calculated based on the material and geometric properties:

$$\mathbf{A}_p = \begin{pmatrix} -0.0965 & 0.1106 & 0 & 0.0055 & -4.5344e-5 \\ 0 & 0 & 1 & 0 & 0 \\ -0.7629 & 0.7629 & -0.0675 & -1.5825 & -0.0040 \\ 0 & 0 & 0 & 0 & 1 \\ 35.7639 & -35.7639 & 0.4075 & -1849 & -1.2910 \end{pmatrix},$$

$$\mathbf{B}_p = \begin{pmatrix} 0.0417 \\ 0 \\ -5.1916 \\ 0 \\ 8.0918 \end{pmatrix}.$$

(38)

The incremental dynamic inverse control method based on FBG compensation was used in the attitude control, and notch filter technology was compared. Finally, the influence of the FBG measurement accuracy on the control system was analyzed.

To compare the control effect and accuracy of different control systems, the performance of the controllers can be evaluated using two indicators [18]: the state deviation rela-

tive to the guidance command and control cost required by the control system. These two indicators can be, respectively, expressed as the integral of pitch-angle deviation and swivel angle, individually:

$$\sum_{\theta_{\text{err}}} = \int_0^t |\varphi_c(t) - \varphi_p(t)| dt,$$

$$\sum_{\delta} = \int_0^t |\delta(t)| dt.$$

(39)

Traditionally, to lower the instability of the control systems caused by elastic vibrations, the control system generally uses a notch filter. The transfer function of a typical notch filter is in the following form [19]:

$$G_{\text{notch}}(s) = \frac{s^2 + 2\xi_z\omega_n s + \omega_n^2}{s^2 + 2\xi_p\omega_n s + \omega_n^2}.$$

(40)

The notch filter was in the position of feedback control in the attitude control system. In the attitude control system, the center frequency ω_n is generally the frequency of the rocket body vibration. For the damping ratios ξ_z and ξ_p , the value usually does not exceed 1. At the same time, to prevent the notch depth from being too large, the values of these ratios were not less than 0.01. In the following work, only the attitude angle and attitude angular rate signals were filtered, and the filtering of the attitude angular acceleration is left as future work.

4.2.1. Modeling of the FBG Measurement System in Flight Environment. In Section 4.1, the transient response of the beam model is used as the “measured data” of the FBG to reconstruct the overall deformation. However, the actual rocket flight is affected by complex flight environment. In addition to measurement error e , there are complex noise in the outputted strain data and a transmission delay between the sensors and the control system. These factors need to be comprehensively analyzed and considered in FBG modeling and controller simulation.

(1) Noise and Transmission Delay Analysis of the FBG Measurement System. The FBG measurement system is mainly composed of a light source, fiber Bragg grating sensors, and FBG demodulator. Affected by the environment and hardware characteristics, each unit may introduce noise sources, resulting in complex additional effects.

To the best of our knowledge, at present, there are few references about noise parameters of onboard FBG measurement systems. In order to simulate the real output signal noise of the FBG measurement system, we investigated and tested the actual FBG measurement system. By analyzing the data of the static FBG sensors, we found that there was background noise in the wavelength signal output by the FBG measurement system, the amplitude limit was 1.6 pm, and the frequency was 1000 Hz. After processing the wavelength variation, the background noise of the strain signal

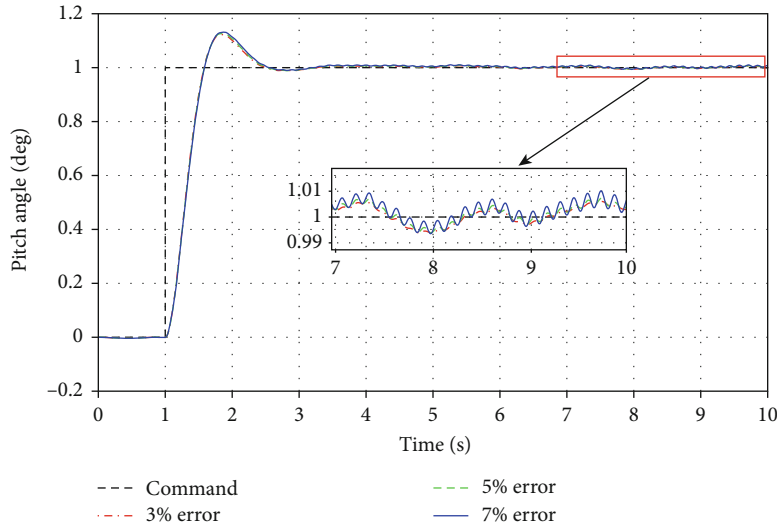


FIGURE 17: Pitch angle response curves of different FBG average errors.

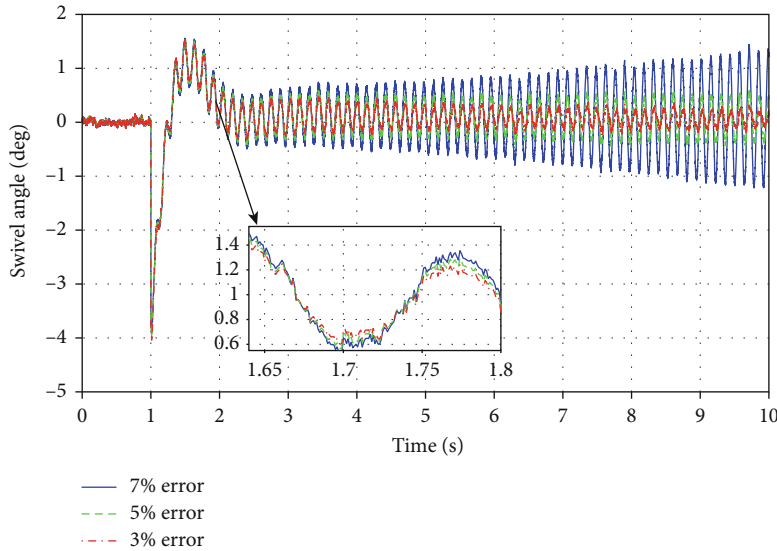


FIGURE 18: Swivel angle curve of different FBG average errors.

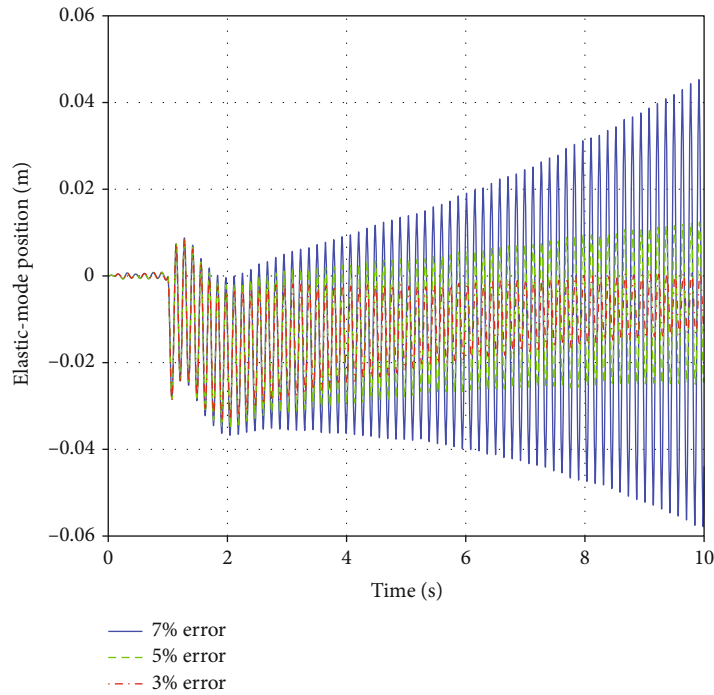
was obtained, the maximum amplitude was about $2\mu\epsilon$, the frequency was about 1000 Hz, and the transmission delay of the measurement system was about 1.5 ms.

However, due to the influence of the complex mechanical and acoustic environment during the flight of the rocket, there may be noise of multiple frequencies. In order to simulate the strain value output by the FBG measurement system during flight, we added three kinds of white noise to the control loop, their sampling times were 0.01 s, 0.001 s, and 0.0001 s, and the maximum amplitude was limited to $2\mu\epsilon$. To simulate the response time delay phenomenon of the sensor, a transmission delay error of 1.5 ms was introduced into the control loop.

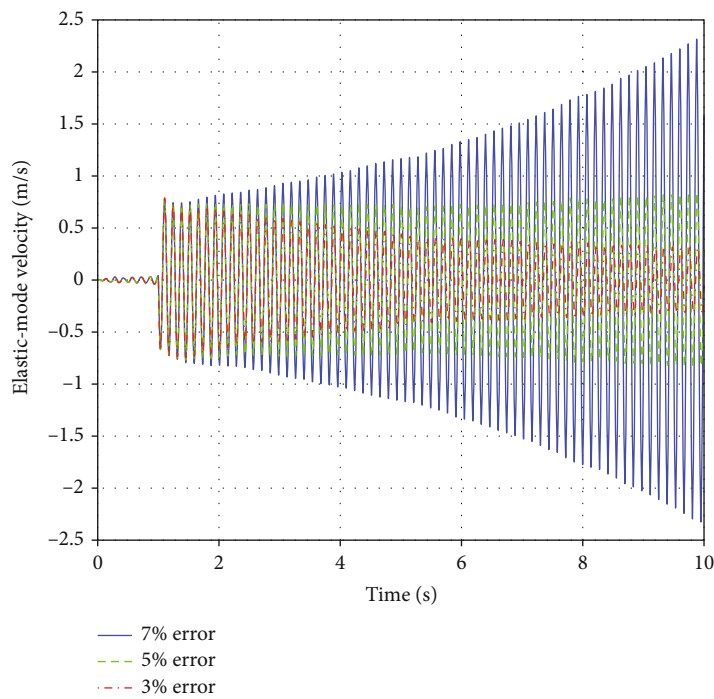
(2) *Influence of Flight Environment on the FBG Measurement System.* During the launcher flight, the temperature and pressure of the environment where sensors are located will

change accordingly due to changes in the flight altitude and the angle of attack. During first-stage flight of the miniature launcher, altitude changes from 0 to 64.9 km. Assuming that sensors are arranged on the surface of the rocket body, according to the U.S. Standard Atmosphere (1976), the temperature changes within the range of $-40\sim 15^\circ\text{C}$ and the pressure change range is within 0.1 MPa.

For changes in external pressure and temperature, a method called reference grating uses a separate reference grating as a temperature and pressure sensor along the fiber path, i.e., gratings that are in thermal and pressure contact with the local structure but shield from strain changes [20]. Since the physical properties of the reference grating and the strain grating are the same, the strain deviation caused by the environmental parameter changes can be well compensated. So, we temporarily ignored the measurement error



(a) Modal coordinates



(b) Modal velocity response

FIGURE 19: Modal coordinates and modal velocity response.

caused by the pressure and temperature changes in the simulation process.

4.2.2. *Incremental Dynamic Inverse Control Based on Fiber Bragg Grating (FBG) Compensation.* According to the model of the liquid launch vehicle flight control system, the incremental dynamic inverse control theory and the improved

method based on FBG compensation proposed in this paper were used to simulate the high-precision attitude control technology of the launch vehicle.

The simulation conditions were as follows:

- (1) The fast loop gain $K_s = 5$, and the slow loop gain $K_q = 4$

- (2) The notch filter parameter ω_n was set to the first-order vibration frequency of the rocket body, and ξ_z and ξ_p were set to 0.012 and 0.57, respectively
- (3) To increase the influence of the elastic effect on the control system, the moment of maximum aerodynamic pressure was selected as the characteristic reference point, and the attitude sensors were placed on the forward end of the second stage, just below the payload adapter ($x_{gyro} = 14.5\text{m}$)
- (4) The control command was set to a 1° step command, and suppose the strain measurement error e was 0

The incremental dynamic inverse control law based on FBG compensation proposed in this paper was used to carry out flight simulations of the launch vehicle and compare the control effects of the rigid body control, uncompensated flexible-body control, and a traditional notch filter. The simulation results of the pitch angle φ and the engine swing angle δ are shown in Figures 10 and 11, respectively. The control performance evaluation indices of each control system are shown in Table 4.

Figure 15(a) shows that for the rigid rocket model ($\eta_i = \dot{\eta}_i = 0$), the system output could track the command attitude in a short time. The maximum overshoot was 12.1%, the adjustment time was 3.7 s (1% error band), and the steady-state error was 0.05%, which verified the effectiveness of the INDI for attitude control of the launch vehicle. For the flexible rocket model, the system output was divergent due to the flexible effect, and the control command could not be tracked (Figure 15(b)). After adding FBG compensation, the maximum overshoot and the adjustment time were basically unchanged, but due to the introduction of the noise error and transmission delay of the FBG measurement system, the steady-state error increased to 0.7%. After using the notch filter, the maximum overshoot increased to 20.7%, and the adjustment time and steady-state error increased significantly. Although the maximum swing angle of the engine was reduced from 4.1 to 3.2 compared to a rigid body after the use of the notch filter, there was a larger amplitude of vibration in the swing angle during the control process (Figure 16).

In summary, the system could still track the command attitude even though there were measurement errors caused by the vibrations of the rocket body after the introduction of the deformation information compensation or the notch filter. However, based on the control effect, the pitching angle response curve and engine swing angle curve with the notch filter exhibited oscillations, and they could not converge to a stable state. Compared with the FBG compensation method, the control precision was higher and the cost was lower.

4.2.3. Influence of FBG Reconstruction Error on the Control System. The simulation was carried out in an accurate system, but there may have been parameter errors in the strain measurements and deformation fitting which led to an inaccurate reconstruction mode. To study the robustness of the control system to the reconstruction error e_r , the simulation was carried out as follows: the FBG reconstruction data had 3%, 5%, and 7% average positive errors, respectively (in this study, the

TABLE 5: Performance results.

	Unit	0% error	3% error	5% error	7% error
$\sum_{\varphi_{err}}$	$^\circ\text{s}$	0.384	0.392	0.401	0.418
\sum_{δ}	$^\circ\text{s}$	1.72	2.23	3.04	4.16

reconstruction data refers to θ_b and q_b , assuming they had the same reconstruction error), the other conditions remained unchanged, and the simulation was repeated. Figure 17 shows the simulation results of the attitude tracking with different reconstruction errors, and Figure 19 shows the modal coordinates and modal velocity responses of the rocket body with different errors.

Figure 17 shows that the pitch angle could still track the command angle after adding 3% and 5% average positive errors. Figures 18 and 19 show that the swivel angle, modal coordinates, and modal velocity reached maxima at 1.0, 1.9, and 1.1 s, respectively, after which they gradually converged to 0. The smaller the e_r was, the faster the convergence speed became. The integrated pitch angle deviation and comprehensive deflection angle increased with the increase in the error (Table 5). When the reconstruction error increased to 7%, the pitch angle curve oscillated by about 0.01° after stabilization and the vibration amplitude increased with time. The swivel angle, modal coordinates, and modal velocity gradually diverged with time.

The simulation results show the following: when the FBG reconstruction error was within a certain range (in this study, the range was 0%–5.2%), the proposed control system could still accurately track the command attitude, but when the reconstruction error was greater than a certain value (5.2%), the mode position and velocity oscillated and diverged, as shown by the blue line.

5. Conclusion

The bending information of a flexible rocket is affected by the attitude control of the rocket body. To address this issue and improve the accuracy of the controller, a deformation reconstruction and high-precision attitude control method of the launch vehicle based on strain measurements was proposed in this paper. The vibration measurement information was combined with the incremental dynamic inverse control to design the control system, and the scheme was simulated and verified. The simulation results showed the following. The deformation reconstruction algorithm based on Legendre polynomials could better estimate the deflection angle and angular velocity caused by vibrations. Compared with the traditional filtering method, the control system with deformation information compensation could track the command attitude more accurately. The FBG reconstruction error was within a certain range, and the control system could still accurately track the command attitude state. The proposed control scheme provided an effective method for the high-precision attitude control of a flexible rocket.

Appendix

A. Miniature Launcher Mass Properties and Geometry

TABLE 6: Properties of the launch vehicle structural model.

Section	Initial coordinate (m)	Length (m)	Thickness (mm)	Mass (kg)	Density (kg/m ³)	Young's modulus (GPa)
Aft stage	0	1.2	5.0	15.0	2780	72.4
LOX 1	1.2	5.6	5.0	266.7	2780	72.4
Fuel 1	6.8	4.4	5.0	213.3	2780	72.4
Inter stage	11.2	1.5	5.0	20.3	2780	72.4
LOX 2	12.7	0.9	5.0	58.3	2780	72.4
Fuel 2	13.6	0.8	5.0	66.7	2780	72.4
Forward stage	14.4	0.2	5.0	10.2	2780	72.4
Fairing	14.6	1.6	3.0	31.4	4430	112

TABLE 7: Additional masses of the launch vehicle model.

Subsystem	Stage 1		Stage 2	
	Mass (kg)	Location (m)	Mass (kg)	Location (m)
Thrust structures	216	0.5	25	11.7
Gimbal system	60	1.0	—	12.2
Valves and lines	50	—	12	—
GNC electronics	—	—	30	14.5
RCS mass	—	—	12	14.5
Payload adapter	—	—	10	14.5
Payload	—	—	105	15.4

Data Availability

The data can be accessed from this manuscript.

Conflicts of Interest

The authors declare that there is no conflict of interest regarding the publication of this paper.

Acknowledgments

We thank LetPub (<http://www.letpub.com>) for its linguistic assistance and scientific consultation during the preparation of this manuscript.

References

- [1] B. N. Suresh and K. Sivan, *Integrated Design for Space Transportation System*, Springer, India, 2015.
- [2] H. D. Choi and H. Bang, "An adaptive control approach to the attitude control of a flexible rocket," *Control Engineering Practice*, vol. 8, no. 9, pp. 1003–1010, 2000.
- [3] H. D. Choi and J. Kim, "Adaptive notch filter design for bending vibration of a sounding rocket," *Proceedings of the Institution of Mechanical Engineers, Part G: Journal of Aerospace Engineering*, vol. 215, no. 1, pp. 13–23, 2005.
- [4] C.-S. Oh, H. Bang, and C. S. Park, "Attitude control of a flexible launch vehicle using an adaptive notch filter: ground experiment," *Control Engineering Practice*, vol. 16, no. 1, pp. 30–42, 2008.
- [5] C. Wei, X. Ju, L. Zhang, and N. Cui, "The modeling and controller design for aeroelastic rocket launcher," *Astronautical Systems Engineering Technology*, vol. 1, no. 1, pp. 21–26, 2017.
- [6] Y. Shtessel and S. Baev, "Active compensation of low frequency flexible modes of crew launch vehicle using sliding mode observers," in *AIAA Guidance, Navigation & Control Conference & Exhibit*, Honolulu, Hawaii, August 2008.
- [7] J. Zhou, Z. Shui, and Z. Ge, "Attitude control for launchers based on robust state observers," *Aerospace Control*, vol. 30, no. 2, pp. 11–16, 2012.
- [8] H. Jiang, B. van der Veen, V. Dolk, D. Kirk, and H. Gutierrez, "Modal estimation by FBG for flexible structures attitude control," *IEEE Transactions on Aerospace and Electronic Systems*, vol. 50, no. 4, pp. 2642–2653, 2014.
- [9] S. G. Calvert and J. Mooney, "Bridge structural health monitoring system using fiber grating sensors: development and preparation for a permanent installation," in *Proceedings Volume 5391, Smart Structures and Materials 2004: Sensors and Smart Structures Technologies for Civil, Mechanical, and Aerospace Systems*, pp. 61–71, San Diego, CA, USA, July 2004.
- [10] S. Rapp, L. H. Kang, U. C. Mueller, J.-H. Han, and H. Baier, "Dynamic shape estimation by modal approach using fiber Bragg grating strain sensors," in *Proceedings Volume 6529*,

Sensors and Smart Structures Technologies for Civil, Mechanical, and Aerospace Systems, San Diego, CA, USA, April 2007.

- [11] L. H. Kang, D. K. Kim, and J. H. Han, "Estimation of dynamic structural displacements using fiber Bragg grating strain sensors," *Journal of Sound and Vibration*, vol. 305, no. 3, pp. 534–542, 2007.
- [12] W. Su, C. K. King, S. R. Clark, E. D. Griffin, J. D. Suhey, and M. G. Wolf, "Dynamic beam solutions for real-time simulation and control development of flexible rockets," *Journal of Spacecraft & Rockets*, vol. 54, no. 2, pp. 403–416, 2017.
- [13] H. Jiang, B. van der Veek, D. Kirk, and H. Gutierrez, "Real-time estimation of time-varying bending modes using fiber Bragg grating sensor arrays," *AIAA Journal*, vol. 51, no. 1, pp. 178–185, 2013.
- [14] H. Gutierrez, B. S. Javani, D. Kirk, W. Su, M. Wolf, and E. Griffin, "Fiber optic sensor arrays for real-time virtual instrumentation and control of flexible structures," *Structural Health Monitoring, Damage Detection & Mechatronics*, vol. 7, pp. 9–22, 2016.
- [15] R. Wu, K. Fu, B. Zheng, and D. Sun, "Error modification of FBG strain sensors bonded on plates," *Optics and Precision Engineering*, vol. 24, no. 4, pp. 747–755, 2016.
- [16] Z. Wang, Q. Wang, and X. Zhang, "An adaptive fuzzy sliding-mode technique for attitude control of launch vehicle," in *2007 International Conference on Mechatronics and Automation*, pp. 1587–1592, Harbin, China, August 2007.
- [17] P. B. Acquatella, W. Falkena, E. J. V. Kampen, and Q. P. Chu, "Robust nonlinear spacecraft attitude control using incremental nonlinear dynamic inversion," in *AIAA Guidance, Navigation, & Control Conference*, Minneapolis, MN, USA, August 2012.
- [18] E. Mooij and D. Gransden, "The impact of aeroelastic effects on the controllability of conventional launch vehicles," in *The 67th International Astronautical Congress*, Guadalajara, Mexico, 2016.
- [19] D. Trotta, A. Zavoli, G. De Matteis, and A. Neri, "Optimal tuning of adaptive augmenting controller for launch vehicles in atmospheric flight," *Journal of Guidance, Control, and Dynamics*, vol. 43, no. 11, pp. 1–8, 2020.
- [20] J.-L. Tang and J.-N. Wang, "Error analysis and measurement uncertainty for a fiber grating strain-temperature sensor," *Sensors*, vol. 10, no. 7, pp. 6582–6593, 2010.